11

Assessment of Abdominal Adiposity and Organ Fat with Magnetic Resonance Imaging

Houchun H. Hu[1], Michael I. Goran[2] and Krishna S. Nayak[1]
[1]*Ming Hsieh Department of Electrical Engineering, Viterbi School of Engineering*
[2]*Childhood Obesity Research Center, Department of Preventive Medicine, Keck School of Medicine*
University of Southern California, Los Angeles, California
United States of America

1. Introduction

As the prevalence of obesity and type II diabetes continues to rise, accurate tools for quantifying abdominal body and organ fat are critically needed to assist researchers investigating therapeutic and preventive measures against obesity and its comorbidities. Fat accumulation in the liver, pancreas, and skeletal muscles are indicators of diabetes, the metabolic syndrome, and obesity. In addition to organ fat, the distribution of abdominal subcutaneous and visceral adipose tissue play critical roles in determining one's metabolic profile and health risks. Rapid comprehensive human body fat quantification remains an unsolved problem and unmet need. Magnetic resonance imaging (MRI) is the most promising modality to address such challenge. MRI is non-invasive, utilizes no ionizing radiation, provides 3D visualization of the anatomy, has immense flexibility in tissue contrast mechanisms, is safely repeatable across longitudinal studies without restrictions, and is applicable to cohorts of all ages, particularly children and adolescents.

This chapter provides the reader with an overview of MRI techniques for measuring abdominal adiposity and organ fat. The described methods are useful in preventive medicine for early detection of health risks, in studies for identifying changes in subcutaneous and visceral adipose tissue volumes due to intervention, such as bariatric surgery and diet, and in comparing trends between gender and ethnicity groups. The chapter is divided into several sections. It begins with a description of MRI principles. This provides the reader with basic knowledge and familiarizes them with terminology. Next, emphasis is placed on specific MRI approaches such as T_1-weighted imaging and magnetic resonance spectroscopy (MRS) as well as state-of-the-art chemical shift imaging (CSI) techniques that are used to assess body and organ fat. Each technique is discussed in detail and compared to its counterparts. Following this description of imaging methodologies, post-processing and image analysis procedures for extracting adipose tissue depot volumes and percent organ fat content from abdominal MRI data using commercially available software are explained. The advantages and disadvantages of each MRI approach with respect to imaging parameters, spatial resolution, subject motion, scan time, and appropriate fat quantitative endpoints are emphasized. The benefits and challenges of contiguous 3D

acquisitions over 2D multi-slice approaches are reviewed. Finally, practical considerations in implementing these methods in the clinical setting are offered, along with an outlook on future fat imaging research. Throughout the chapter, illustrative figures accompany each section to highlight the topics.

2. Basic principles of magnetic resonance imaging

Detailed MRI physics are available for the casual (Hashemi & Bradley, 1999) and technical readers (Bernstein et al., 2004; Haacke et al., 1999; Vlaardingerbroek & den Boer, 1999).

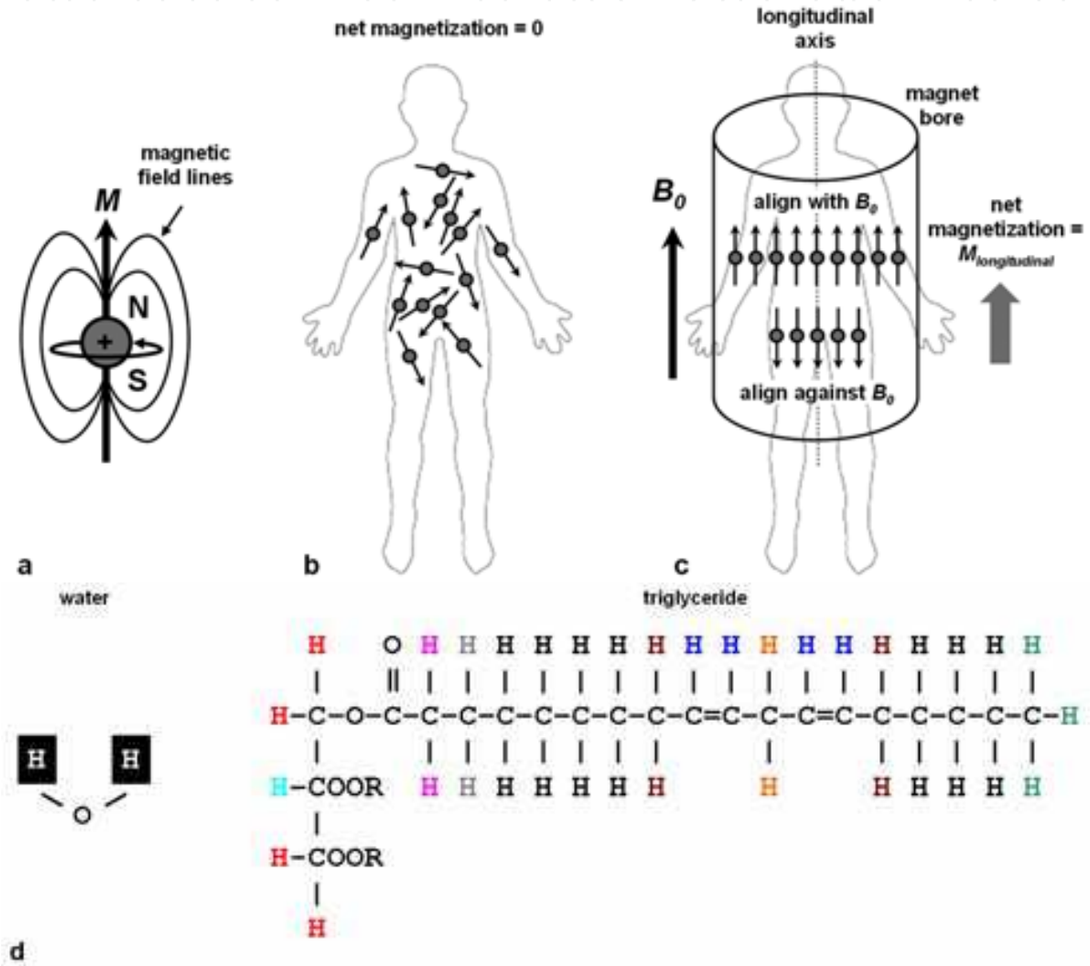

Fig. 1. Magnetization. (a) A hydrogen atom, or proton spin, exhibits a magnetic dipole M, due to the spinning motion of its positive nucleus. The dipole is similar to a bar magnet with "North (N)" and "South (S)" poles. (b) Spins are randomly oriented without the presence of a B_0 field and gives rise to no net magnetization. (c) Dipoles either align with or against the B_0 field in its presence, with a slight preference for the former. A measurable magnetization, $M_{longitudinal}$, is thus generated. (d) Water and fat (triglycerides) are the most common hydrogen-containing molecules. For fat, colors represent hydrogens with different local chemical environments. Figure (d) courtesy of G. Hamilton, Ph.D., University of California San Diego. Schematic presented for illustration only and is not drawn to scale.

2.1 Signal origin, magnetization, and precession: The "M"

The signal in MRI arises from the nucleus of an atom, which consists of one or more positively charged protons. Figure 1a illustrates a naturally spinning nucleus, which can be considered as a charged particle in motion (e.g. an electric current). The movement of this electric current, albeit an infinitesimally small one, produces a magnetic dipole M about the nucleus. While the inherent magnetic dipole of a single atom is small, a large population of atoms in an object or human body can be significant and detectable. The magnetization of hydrogen whose nucleus consists of a single proton (^{1}H) is frequently measured in MRI, due primarily to its high natural abundance in organic life forms. The two most common hydrogen-containing molecules are water and fat (e.g. triglycerides), as shown in Figure 1d. Their magnetization signals within an imaging object or patient are detected, excited, measured, and reconstructed into diagnostic images.

The superconducting MRI magnets used for human imaging generates a magnetic field (B_0) strength between 0.5 and 3.0 Tesla (T). Routine imaging is performed at 1.5T, and in more recent years at 3.0T. By comparison, these strengths are much greater than the natural North-South magnetic fields of Earth's poles, which varies between 0.3 and 0.6 Gauss (G), where 1T=10,000G. The B_0 field is oriented along the longitudinal axis of the magnet bore, as shown in Figure 1c. Prior to placing a subject within the magnet bore, each proton spin within a population has its magnetic dipole oriented in a random direction (Fig. 1b). The net magnetization of this population is zero and not detectable. Figure 1b illustrates spin behaviors after the subject enters the B_0 field. The magnetic field forces the individual dipoles to either align with or against B_0. Only a small fraction of spins preferentially align with B_0 than against it. Nevertheless, it is this slightly greater population of dipoles that align with B_0 and the abundance of hydrogen atoms *in vivo* that is responsible for producing a measurable net signal. Since this net magnetization is oriented along the longitudinal axis of the magnet bore, it is referred to as $M_{longitudinal}$. With higher B_0 fields, the proportion of aligned spins increases and gives rise to a larger $M_{longitudinal}$ and hence a stronger signal.

Interactions between the magnetization and the B_0 field causes precession. The Larmor frequency or rate of precession f_{Larmor} is determined by Equation 1, where $\gamma/(2\pi)$ is the gyromagnetic ratio of the nuclei of interest. For protons, it is 4,257 Hz/ G.

$$f_{Larmor} = \gamma / (2\pi) \cdot B_0 \tag{1}$$

The Larmor frequency is nuclei specific and linearly proportional to B_0. At B_0 = 1.5T, proton f_{Larmor} is 63.86 MHz; at 3.0T, it doubles to 127.6 MHz (1MHz = 10^6 Hz, 1Hz=1 cycle/ second). It is precession, the continuous motion of spin magnetization M at the Larmor frequency that induces signals needed for image generation. Thus, analogous to a radio transmitter and receiver, MRI signal detection is based on frequency, and as will be discussed later, it is precisely the Larmor frequency difference between hydrogens in water and fat that underpins several approaches to body and organ fat quantification.

2.2 Radiofrequency excitation and relaxation: the "R"

Once $M_{longitudinal}$ is generated, it must be tipped, or nutated, into the orthogonal transverse plane in order for signals from precessing spins to be detected by local receiver coil(s). This is shown in Figure 2. The nutation from $M_{longitudinal}$ to $M_{transverse}$ is accomplished through radiofrequency (RF) pulses that are applied on resonance at the Larmor frequency. In the figure, a 90º nutation or excitation is shown. However, an arbitrary value can be used. The angle of nutation is denoted by α and is referred to as the flip angle. Just as the RF excitation

pulse is applied on resonance at the Larmor frequency to most efficiently nutate $M_{longitudinal}$, the receiver coil(s) are similar tuned to the Larmor frequency to detect $M_{transverse}$.
After $M_{transverse}$ is created and the RF pulse is turned off, the spins will gradually begin to "relax". Two simultaneous and independent relaxation processes occur. First, the signal will recover towards the longitudinal axis, progressively restoring the $M_{longitudinal}$ vector to its original state prior to RF excitation. The rate recovery is denoted by the T_1 spin-lattice term, an exponential constant. Second, spins in the transverse plane will gradually lose signal coherence. This causes a progressive reduction of $M_{transverse}$ at an exponential decay rate of T_2, also known as spin-spin relaxation. T_1 and T_2 values are material, tissue, and B_0 dependent (De Bazelaire et al., 2004; Stanisz et al., 2005).

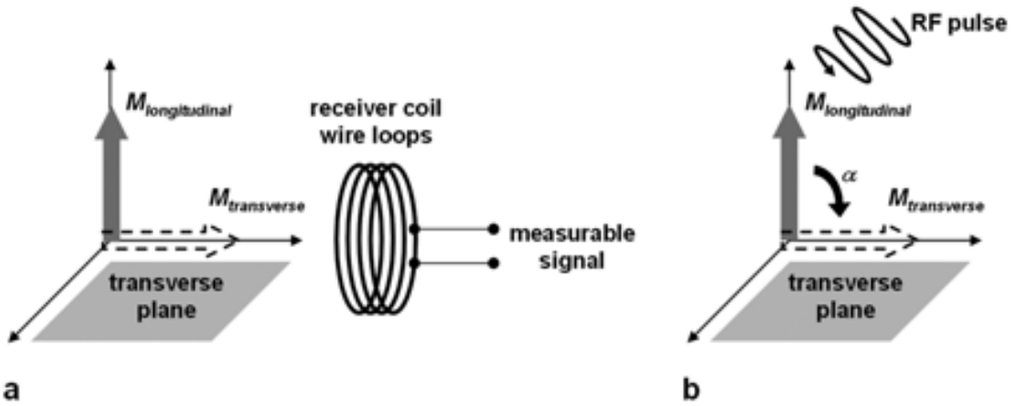

Fig. 2. RF excitation. (a) $M_{longitudinal}$ does not induce a signal in the receiver coil. In order for a measurable signal to be generated, $M_{longitudinal}$ must be nutated into the orthogonal plane (dashed arrow) to form $M_{transverse}$. (b) Nutation is accomplished via excitation by an RF pulse applied on resonance at the Larmor frequency. The duration and amplitude of the pulse determines the angle of nutation, or flip angle α. A 90º example is shown.

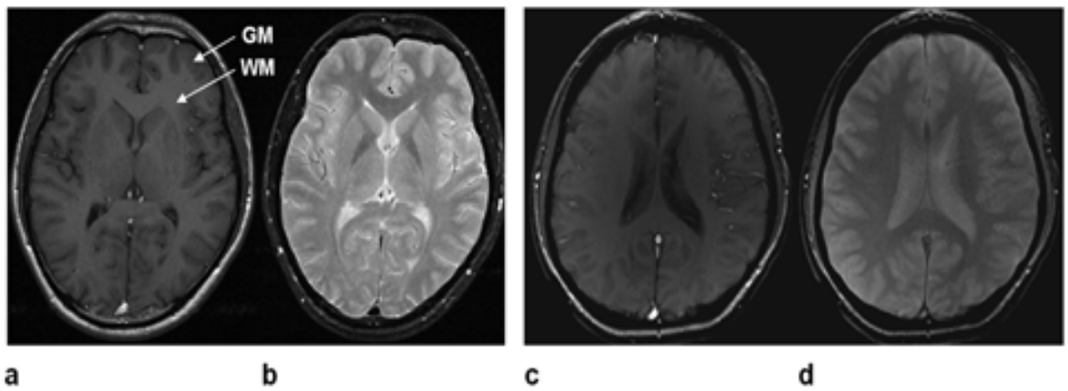

Fig. 3. Tissue contrast. Axial brain sections acquired with (a) TR=400 msec, TE=14 msec; (b) TR=2000 msec, TE=80 msec in one subject while keeping the flip angle constant. (a) A T_1-weighted image where gray matter (GM) is darker than white matter (WM). (b) A T_2-weighted image, where tissue contrast has been inverted and GM is brighter than WM. Axial brain sections acquired with (c) flip angle of 30 degrees and (d) 5 degrees in another subject, while keeping TR and TE constant. Note again differences in tissue contrast.

In an MRI experiment, RF pulses are repeated in the form of a pulse sequence to gather adequate data for each imaging slice of interest. After each RF excitation, a signal or echo is measured at a specified echo time (TE). The time between successive RF excitations is the repetition time (TR). By varying the flip angle, TR, and TE, an operator has immense flexibility over tissue signal contrast in the resultant image. Figure 3 illustrates two axial sections of a human brain, acquired with different pairs of TR and TE values. Note that the signal contrast between gray and white matter changes. TR and TE pairs that exploit the difference in T_1 values between tissues yield T_1-weighted images (Fig. 3a), where white matter (shorter T_1, faster recovery) is brighter than gray matter (longer T_1, slower recovery). On the contrary, TR/ TE pairs that exploit differences in T_2 yield T_2-weighted images (Fig. 3b), where white matter (shorter T_2, faster decay) is darker than gray matter (longer T_2, slower decay). Similar tissue contrasts can be achieved by changing only the flip angle (Fig. 3c, d).

2.3 Magnetic gradients, k-space, and the Fourier transform: the "I"

In a pulse sequence, each echo gathers signal contrast and spatial information about the imaging object and its spin ensemble. A pulse sequence (Fig. 4) contains not only the RF component, but also three magnetic gradients, G_{slice}, G_{phase}, and G_{read}. These gradients perturb the B_0 field linearly as a function of distance. In synchrony with G_{slice}, a RF pulse can excite an isolated section of the imaging object (e.g. the head, abdomen, or knee). This is known as volume or slice-selection. G_{phase} and G_{read} then provide information on the spatial locations of spins from the excited section by establishing a one-to-one relationship between their locations and their unique precessing frequencies and phases (spatial-encoding). Aligning the three gradients in various combinations yields the desired image orientation.

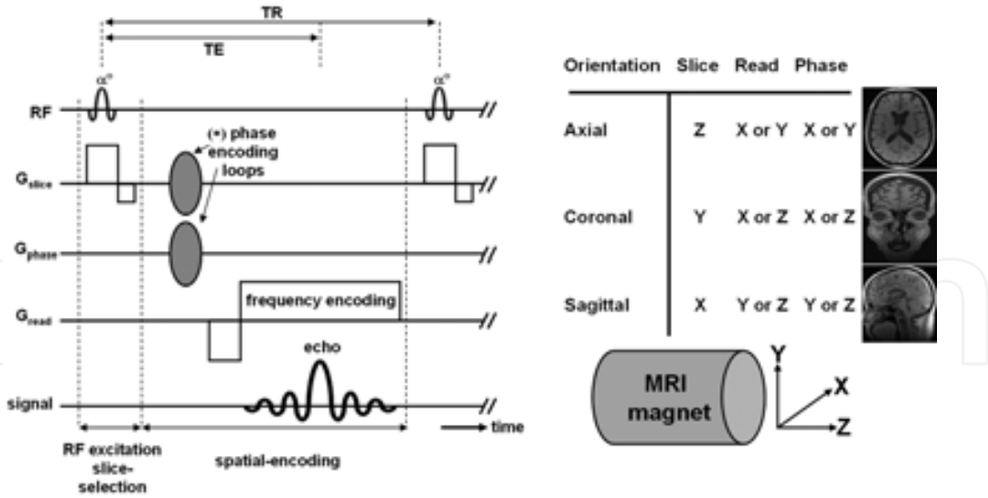

Fig. 4. A pulse sequence diagram. Gradient G_{slice} is applied in conjunction with the RF pulse to specifically excite a desired section of the imaging object at a given orientation. This is followed by 2D or 3D spatial-encoding (*), where locations of spins are determined based on their precessing frequency and their phase accrual in the presence of G_{read}, G_{phase}, and G_{slice}.

Each acquired echo provides a snapshot, or "view" of the underlying image. By iterating through multiple spatial (frequency and phase) encoding loops, differential "views" of the

imaging object are obtained. Each echo is an oscillatory function that represents the sum of a spin ensemble observed from a particular "view", and each of the involved spins are precessing at a slightly different gradient-tuned frequency and phase. To separate the signal into its individual components, each echo is first stored as a line of data points in the spatial frequency domain, or *k*-space. Once all echoes are acquired, a Fourier Transform (FT) operation generates the image (Fig. 5).

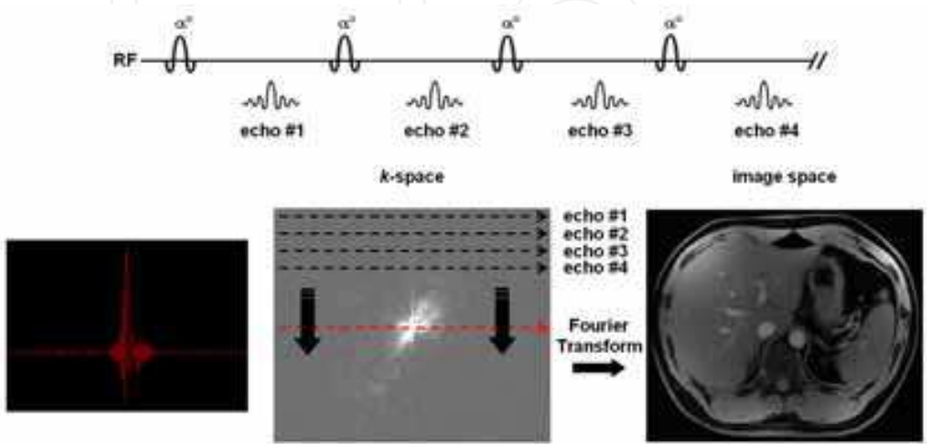

Fig. 5. Image formation. A pulse sequence collects echoes and fills the data in *k*-space after each RF pulse. A Fourier Transform yields the net image result after the pulse sequence iterates through multiple spatial-encoding "view" loops. An echo example is shown in red.

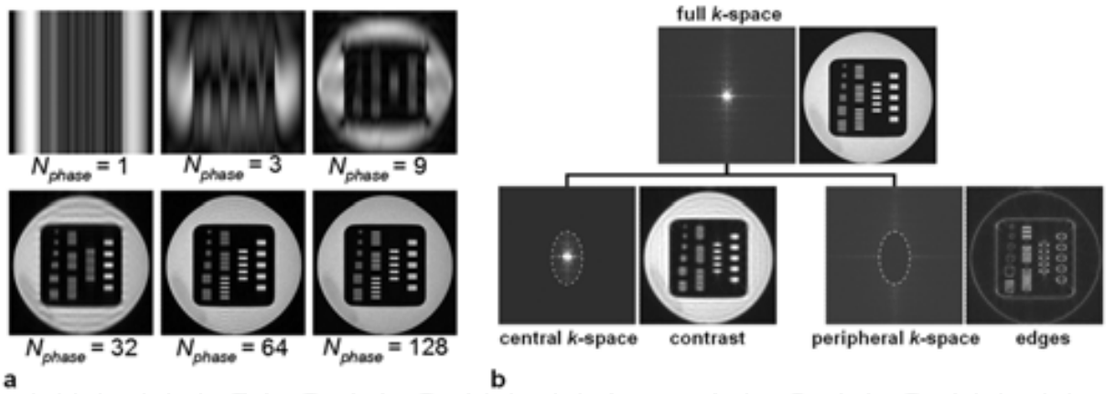

Fig. 6. *k*-space and resolution. (a) A set of images with varying numbers of "views". Resolution improves with more "views". (b) *k*-space can be considered in two parts, a central region containing low-spatial-frequency data inside the dashed ellipse, and a high-spatial-frequency region outside the ellipse. Images show that low-spatial-frequencies give rise to gross contrast, while high-spatial-frequencies contribute to edges and details. When an echo is acquired, it samples both central and peripheral *k*-space.

2.4 Field of view, spatial resolution, and acquisition time

Field of view (FOV) describes the size of the imaging volume and is set by the MRI operator. Spatial resolution refers to the physical dimensions of each 2D pixel or 3D voxel. Smaller dimensions provide greater spatial resolution and resolving power to delineate fine

structures. Spatial resolution is determined by the number of acquired *k*-space data samples (*N*), and can be computed as the ratio of FOV and *N* along each axis. Higher resolution usually demands a greater number of samples, which consequently implies a longer acquisition time of the MRI experiment. This is because it typically takes one TR repetition to acquire each of the N_{phase} and N_{slice} phase-encoding "views". Figure 6a illustrates a series of images of a circular object. N_{read} was set constant (horizontal axis) while N_{phase} (vertical axis) was varied. With only one phase-encoding "view", vertical spatial resolution is non-existent. With nine "views", the circular outline and embedded parallel bars become visible. With 32, 64, and 128 "views", the detail of the bars are improved. Figure 6b illustrates a key property of *k*-space. A full *k*-space data set is shown along with its image. If only central *k*-space is reconstructed, the resultant image exhibits the overall shape and signal contrast of the object, but is blurry and lacks spatial detail. Conversely if only the peripheral data points are reconstructed, the resultant image is devoid of any signal contrast, but shows edge detail. Thus, both central and peripheral *k*-space are critical for high image quality.

3. Magnetic resonance imaging of fat

As the prevalence of obesity and type II diabetes continue to rise (Flegal et al., 2010), evidence has attributed obesity-related health risks to the accumulation of subcutaneous and visceral adipose tissue (SAT, VAT) and ectopic organ fat (Choudhary et al., 2007; Despres et al., 2008). Non-invasive assessment of body and organ fat has become an important component in obesity research and fat measures are useful as biomarkers to stratify risks and evaluate the efficacy of therapies.

Many methods have been historically available for body fat assessment (Ellis, 2000; Mattsson, 2006). Anthropometry, hydrodensitometry, air displacement plethysmography (ADP), bioelectric impedance (BIA), and dual energy X-ray absorptiometry (DEXA) have been widely used. The first four are indirect techniques because they measure body density or resistance, which are then converted into percent body fat using generalized equations (Jackson, 1982). Hydrodensitometry and ADP are limited to estimating total body fat, while BIA and DEXA are limited to total and regional body fat measures. Most importantly, these indirect methods are not able to differentiate between SAT and VAT or identify ectopic fat.

An increased utilization of computed tomography (CT) (Goodpaster et al., 2000, Kvist et al., 1988; Seidell et al., 1990), quantitative magnetic resonance (QMR) (Napolitano et al., 2008), and particularly MRI for body fat assessment (Abate et al., 1997; Berglund et al., 2010; Brix et al., 1993; Kullberg et al., 2009; Lancaster et al., 1991; Machann, et al., 2005; Ross et al., 2000; Schick et al., 2002; Siegel et al., 2007; Thomas et al., 2005;) has been reported in recent years. Along with DEXA, CT, QMR, and MRI are direct techniques because they identify fat based on the tissue's unique properties and signals in each modality. QMR does not yield images and is limited to measuring total body fat. In contrast, CT and MRI can differentiate SAT and VAT with multi-dimensional images. However, only MRI, with its sensitive contrast mechanisms for water and fat-based tissues, can accurately quantify ectopic fat. MRI is emerging as a comprehensive tool for fat quantification. The following sections describe fundamental MRI concepts that underpin T_1-weighted imaging, MR spectroscopy (MRS), and state-of-the-art chemical shift imaging (CSI).

3.1 T_1-Weighted MRI

As discussed in Section 2.2, MRI signal intensities are influenced by many factors including proton density, tissue-specific relaxation rates, the flip angle, and pulse sequence timings.

The T_1 of fat is one of the shortest amongst tissues *in vivo*. This indicates a very rapid recovery of its longitudinal magnetization between successive RF excitations. Therefore, by using a T_1-weighted sequence, strong tissue contrast can be achieved between short-T_1 fat tissues and muscles and organs with longer T_1 values (Fig. 7). Bright fat can thus be easily identified and delineated by simple signal intensity thresholding (e.g. cutoff) from darker structures. T_1-weighted sequences are very common in clinical MRI and are a part of nearly every protocol and anatomy. They have been used by several investigators as the standard workhorse tool for assessing SAT and VAT distributions (Machann et al., 2005; Ross et al. 2000; Siegel et al., 2007). T_1-weighted sequences are available as standard software on all commercial MRI scanners (GE, Philips, Siemens, Hitachi, and Toshiba) and can be easily implemented by the operator. Tissue T_1 values increase slightly with B_0 field, such that optimization in pulse sequence parameters are needed to maintain comparable tissue contrast between magnetic field strengths.

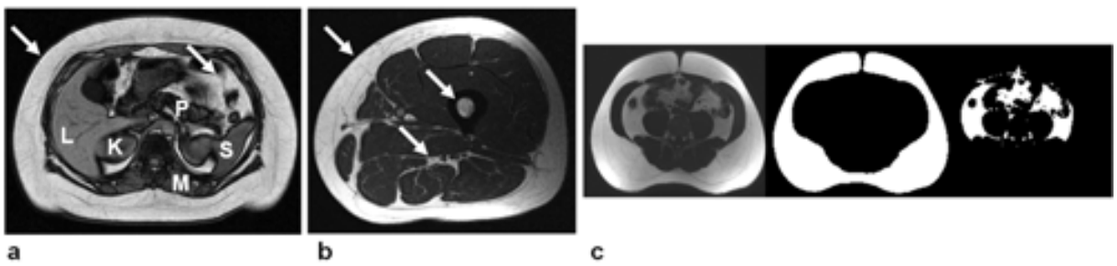

Fig. 7. T_1-weighted MRI. Examples in the (a) abdomen and (b) thigh, demonstrating the high signal intensities of fat *in vivo* (arrows: SAT, VAT, bone marrow, intermuscular fat) in contrast to darker muscles and organs (L: liver, P: pancreas, K: kidneys, M: muscle, S: spleen). (c) A high signal intensity threshold of an abdominal T_1-weighted image easily identifies fat pixels. Intensities with values below the set threshold are "discarded" and set to zero. For well-optimized T_1-weighted pulse sequences, this simple step can be quite robust in identifying abdominal SAT (middle) and VAT depots (right).

3.2 Single-voxel magnetic resonance spectroscopy

Single-voxel MRS has been the gold-standard for ectopic fat quantification (Hamilton et al., 2009; Kim et al., 2008; Lingvay et al., 2009; van Werven et al., 2009; Weis et al., 2008). Unlike MRI, MRS usually does not provide anatomical information in the form of an image. It instead yields a precise spectrum of chemical composition within one voxel. MRS relies on chemical shift, which refers to differences in the Larmor frequencies of water and fat protons (Fig. 8). Water protons from (-OH) hydroxyl groups are characterized by a spectral peak at 4.7 ppm (parts-per-million). In contrast, the predominant protons of triglycerides are from the $(-CH_2)_n$ methylene groups (black H in Fig. 1d). Due to different chemical environments surrounding the protons (oxygen in water versus carbon in triglycerides), methylene protons have a slightly lower resonant frequency. The frequency separation between water and the methylene fat peak is linearly proportional to B_0, such that larger chemical shift separations are achieved with increasing field strengths. At 1.5 and 3.0 Teslas and body temperature, the water-fat chemical shift is approximately 220 and 440 Hz, respectively (Brix et al., 1993; Cassidy et al., 2009; Ren et al., 2008). Note that this frequency difference is miniscule in comparison to the MHz Larmor values. Nevertheless, water-fat chemical shift is detectable via MRS and the resulting spectrum provides an intuitive visualization of the

presence and relative quantity of chemical species. MRS packages are available on most commercial MRI scanners and typically require some operator expertise to implement.

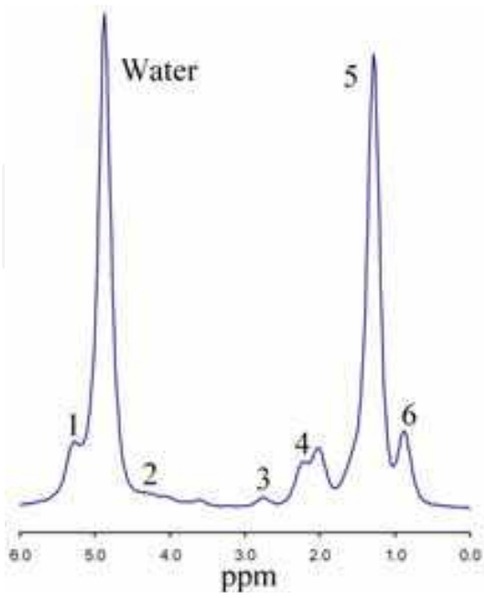

Peak	ppm	Assignment
1	5.3	-CH=CH- -CH-O-CO-
Water	4.7	H_2O
2	4.2	$-CH_2-O-CO-$
3	2.75	$-CH=CH-CH_2-CH=CH-$
4	2.1	$-CO-CH_2-CH_2-$ $-CH_2-CH=CH-CH_2-$
5	1.3	$-CO-CH_2-CH_2-$ $-(CH_2)_n-$
6	0.9	$-(CH_2)_n-CH_3$

Fig. 8. Example of a spectrum from ^{1}H MRS containing water and fat. The water peak is at 4.7 ppm. The fat methylene peak (#5) is shifted 3.4 ppm downfield, at 1.3 ppm. While water is a symmetrical molecule and has a true single peak, fat exhibits additional minor peaks from other moieties, some of which are in close proximity to the water peak. The area under each peak represents the amount of each species present, such that a fat:water ratio (e.g. a fat fraction) can be measured. The Larmor frequency separation between water and fat can be computed by multiplying the ppm difference by the right-side of Equation 1. Color notation corresponds to Figure 1. Figure courtesy of G. Hamilton, Ph.D., University of California San Diego.

3.3 Frequency-selective MRI

Since MRI involves RF pulses tuned to specific resonant frequencies, a novel technique that exploits the Larmor difference between water and fat to quantify SAT, VAT, and intermuscular fat has been developed (Kaldoudi et al., 1993; Machann J et al., 2003; Peng et al., 2007, Schick et al., 2002). One approach is to selectively excite fat spins by tuning a narrow bandwidth RF pulse specifically to fat's resonant frequency. As a result, only fat protons are nutated and detected by signal receivers while those of water remain in the longitudinal plane. The encoded data and image exhibit only signals from fat and the appearance resemble T_1-weighted contrast where fat appears recognizably bright (Fig. 9). The sharp contrast between water and fat-dominant tissues and organs readily facilitates thresholding and fat volume quantification. Selective-fat-excitation and water-suppression are terms used interchangeably to refer to this technique in literature.

A disadvantage of selective-fat-excitation is that the narrow bandwidth RF pulse can only account for the methylene fat peak and minor peaks that are in its close proximity. The fat peaks near water are neglected. This issue limits the applicability of frequency-selective MRI to SAT and VAT quantification only, and not ectopic fat content. Frequency-selective

techniques can be implemented on all commercial scanners. The method works well at 1.5T, but can be unreliable at higher fields due to its sensitivity to B_0 inhomogeneities. B_0 inhomogeneity refers to unknown object-dependent and spatially-varying deviations of the magnetic field from its intended value, and can cause unintentional resonant frequency drifts on the order of 10^2 - 10^3 Hz. Inhomogeneities arise from manufacturing imperfections, perturbations by metals, and the mere placement of a human inside the magnet bore. They are quite significant around air-tissue-bowel interfaces. B_0 inhomogeneity, also known as off-resonance, globally shifts the ppm locations (and Larmor frequencies) of water and fat peaks such that they are no longer at 4.7 and 1.3 ppm, respectively. However, the difference between them remains unchanged at 3.4 ppm. In the presence of significant B_0 inhomogeneity, an RF pulse intended for fat's resonance can erroneously excite water's resonance. Although higher field strength leads to greater water-fat peak separation, the worsening B_0 inhomogeneity counteracts the benefit and degrades overall performance.

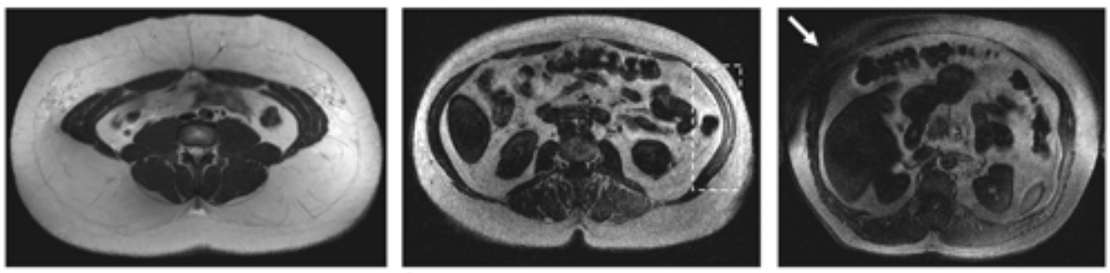

Fig. 9. Frequency-selective MRI. Three slices are shown acquired at (a) 1.5T, and (b, c) 3.0T. In (a), SAT and VAT exhibit high signal intensity, in contrast to water-dominant muscles and organs. In (b), the dashed box encloses the left oblique and transversus abdominis muscles. There is appreciable signal from the muscles, in comparison to the darker right side. Due to B_0 inhomogeneity, selective-fat-excitation was ineffective in this region. In (c), performance is severely hindered in the right anterior SAT region (arrow). Significant B_0 inhomogeneity has caused the selective-fat-excitation RF pulse to *suppress* fat signal.

3.4 Chemical shift MRI

Chemical shift imaging (CSI) integrates sensitive water-fat spectral detection from MRS with imaging (Bley et al., 2010; Hood & Ho, 1999; Ma, 2008). CSI consists of a family of approaches that have been developed over the past 25 years. Dixon was the first to demonstrate that by controlling the echo time when data was acquired after RF excitation, the net detected MRI signal can comprise either of water and fat in-phase (IP=W+F, aligned, phase=0 degrees) or out-of-phase (OP=W-F, anti-aligned, phase=180 degrees), as illustrated in Figure 10 (Dixon, 1984). Dixon recognized that by using this two-point (IP and OP) approach, separated water and fat images could be obtained by image algebra (Cassidy et al., 2009). By reconstructing separated water and fat images, a subsequent percent fat fraction map (fat:water ratio) can be computed, which would facilitate measurement of fat accumulation in organs on a voxel-by-voxel basis. Intuitively, one can realize that for a voxel containing only water or fat, its net signal will be the same on IP and OP acquisitions as one component's signal will be zero. In contrast, a voxel containing both water and fat will have different signals from the two acquisitions (Fig. 11). Recent developments in water-fat separation and image reconstruction algorithms have advanced the traditional two-point

Dixon method beyond IP/ OP to arbitrary echo time choices (Berglund et al., 2011; Bydder et al., 2011; Eggers et al., 2011; Ma, 2008; Xiang, 2006).

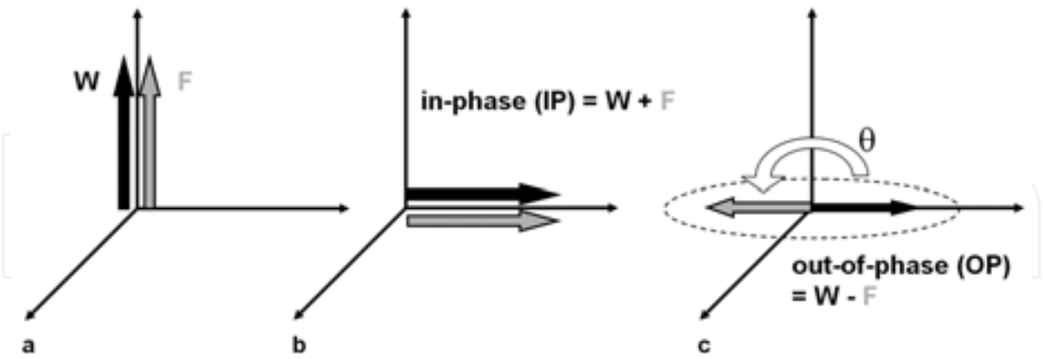

Fig. 10. Two-point Dixon MRI. (a) Before RF excitation, water (W) and fat (F) magnetizations are along the longitudinal axis. (b) Immediately after RF excitation, the transverse magnetizations are in-phase. An echo acquired at this point would reflect a net signal of W+F. (c) With the signal receivers tuned to the Larmor frequency of water, the slower precessing chemically-shifted fat signal will accrue a phase of 180 degrees, or OP, with respect to water after some time. An echo acquired at this point would reflect a net signal of W-F. As time proceeds, the signal will become IP and OP periodically. At 1.5T, the periodicity is 2.4 msec; at 3.0T, it is 1.2 msec. For this approach, only the methylene fat peak is considered. Note in (c) that both vectors are smaller in amplitude, due to T_2 relaxation.

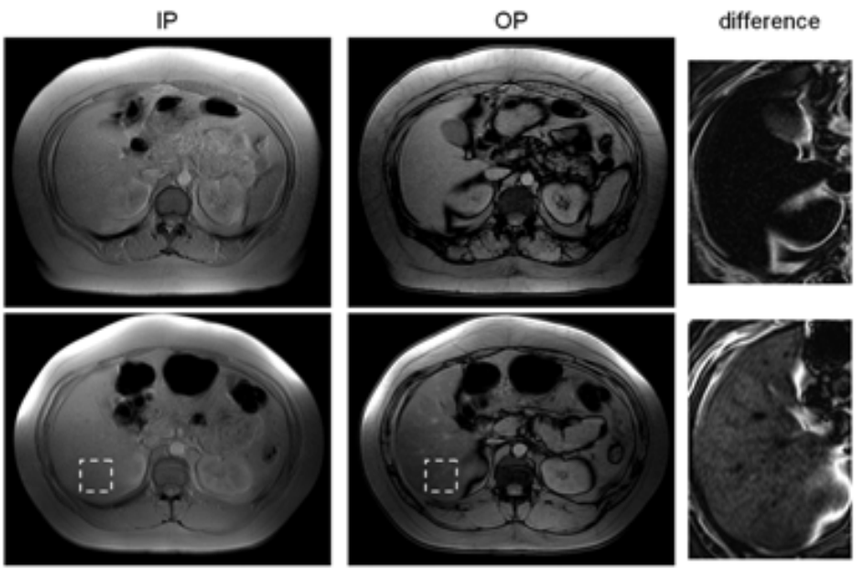

Fig. 11. Two-point Dixon MRI. In-phase (IP) and out-of-phase (OP) images from two subjects are shown. In the first subject (top row), the signal intensities within the liver between IP and OP images are similar. This signifies very little presence of hepatic fat. In the second subject (bottom row), the liver signal intensities is lower in the OP image (dashed regions). This indicates presence of hepatic fat. The difference image of the top subject is nearly zero in the liver, whereas the lower subject shows appreciable signal. As determined by MRS, the hepatic fat fractions of the subjects were 3.4% and 21.2%, respectively.

CSI has evolved significantly over the past decade due to strong motivation by clinical interest and research in obesity and its comorbidities, particularly fatty liver disease (Bley et al., 2010; Cassidy et al., 2009; Ma, 2008). More robust and improved techniques have been developed to incorporate B_0 inhomogeneity estimation into the water-fat separation algorithm. These variants typically require three or more TE measurements (e.g. three-point Dixon). Modern CSI approaches have also addressed the problem of water-fat signal ambiguity (Hussain et al., 2005), which refers to the inability of early two-point methods to determine whether fat or water is the predominant specie present in a voxel. In other words, a voxel contain x% fat and (100-x)% water can be indiscernible from a voxel containing x% water and (100- x)% fat (e.g. there is ambiguity about the 50% fat fraction apex). Many recent literature reports have validated CSI in measuring liver fat fraction (Kim et al., 2008; Guiu et al., 2009; Hussain et al, 2005; Hu et al., 2010; Meisamy et al., 2011; O'Regan et al., 2008; Yokoo et al., 2009). While CSI pulse sequences are not difficult to implement, they often require technician involvement and manufacturer support in establishing appropriate protocols. CSI software is available on new commercial MRI platforms as clinical or research-dedicated software.

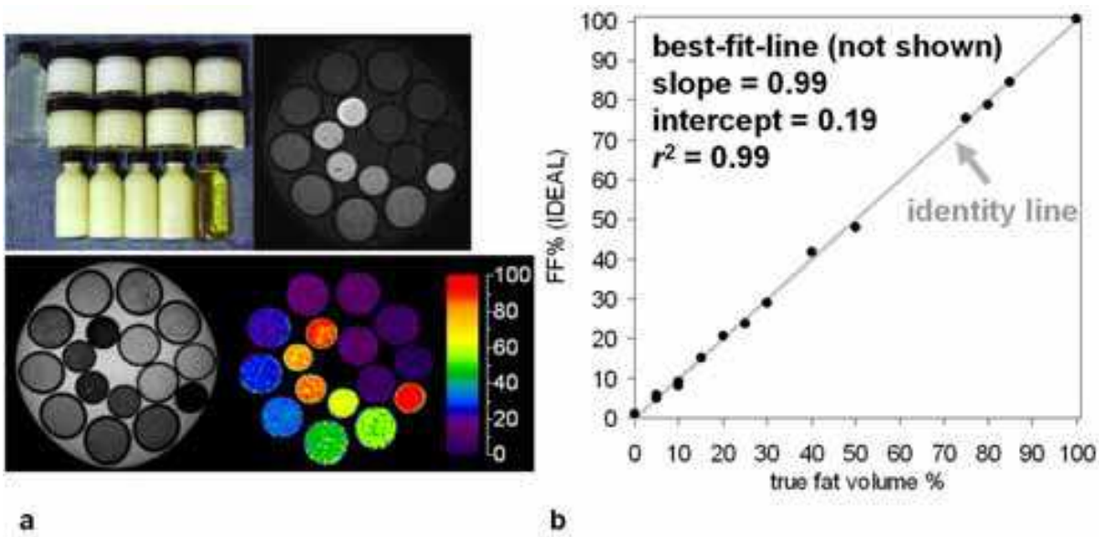

Fig. 12. IDEAL fat fraction (FF) MRI. (a) Oil-water emulsions, ranging in percent volume oil from 0% (clear bottle) to 100% (transparent yellow bottle) are shown. IDEAL reconstructed fat-only and water-only images in the upper right and bottom left panels, respectively, along with the colorized FF map. The bottles are in a water-filled dish. (b) Correlation of true fat volume fraction against the mean FF from IDEAL. Excellent agreement is achieved.

Recent advances in CSI have led to the development of comprehensive methods such as IDEAL (Iterative Decomposition with Echo Asymmetry and Least squares) (Reeder et al., 2007). IDEAL is a generalization of the multi-echo Dixon model (a three to six-point Dixon approach) and has been successfully demonstrated at both 1.5 and 3.0 Tesla. At both field strengths, IDEAL is robust to B_0 inhomogeneity, addresses water-fat signal ambiguity such that percent fat fractions can be determined across the 0–100% range without ambiguity (Bernard et al., 2008; Hines et al., 2009), accounts for T_1 and T_2 relaxation of water and fat (Bydder et al., 2008; Chebrolu et al., 2010; Liu et al., 2007), and models the multiple peaks of fat with an accurate spectrum (Hernando et al., 2010; Yu et al., 2008). The latter is a critical methodological advancement in accurate ectopic fat quantification (percent organ fat

fraction) as it accounts for nearly all of the minor fat spectral peaks in addition to the primary methylene peak. A single IDEAL acquisition yields not only reconstructed fat-only and water-only images and accurate fat fraction maps [$F/(F+W)$], but also IP and OP series that are useful for anatomical definition. IDEAL has been rigorously validated against MRS and other CSI methods in the liver (Hu et al., 2010; Reeder et al., 2009; Reeder & Sirlin, 2010; Meisamy et al. 2011). IDEAL and its variants have been used to study brown and white adipose tissues (Hu et al., 2010) and fat accumulation in the heart (Kellman et al., 2010). IDEAL is a patented and proprietary software that is commercially available from GE Healthcare. Figures 12-14 highlight the robustness and utility of IDEAL in visualizing and quantifying tissue fat fraction and organ fat content.

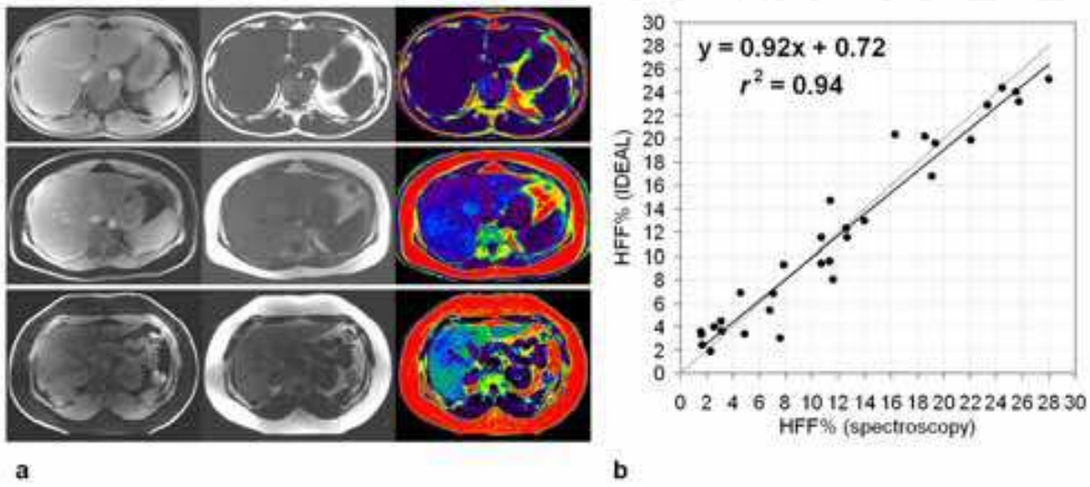

Fig. 13. IDEAL fat fraction (FF) MRI. (a) IDEAL-reconstructed water-only, fat-only, and colorized FF maps of the liver in three subjects are shown. Same color bar as Fig. 12. It is evident that the three subjects have varying degrees of fat accumulation in the liver, beginning with a low 3% in the top case (dark purple), to approximately 23% in the middle case (dark blue), to more than 40% (light blue, green) in the lower case. Note also greater SAT volumes in the middle and lower cases. (b) Excellent correlation in hepatic FF was achieved between IDEAL MRI and reference MRS (n=31). The identity line is in gray.

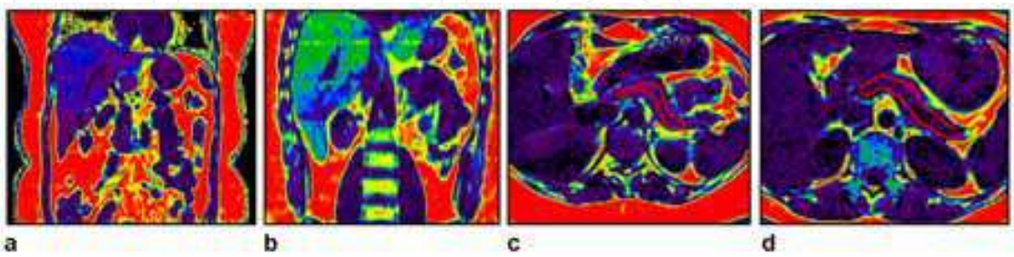

Fig. 14. IDEAL fat fraction (FF) MRI. (a, b) IDEAL-reconstructed FF maps of the liver in two subjects, shown in the coronal orientation. The 3D nature of IDEAL data facilitates visualization of the FF map from any perspective. Same color bar as Fig. 12. Note that SAT and VAT distributions can be clearly seen, along with varying degrees of fat accumulation in the liver. (c, d) Two examples of pancreas (red outline), with an average 11% and 5.1% percent FF within the traced regions, respectively.

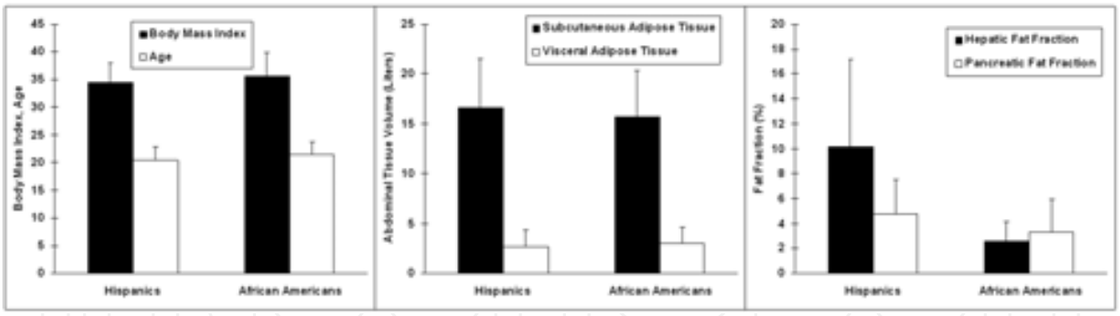

Fig. 15. Data from a cohort of age- and BMI-matched Hispanics and African Americans (n=13 in each group) using IDEAL MRI. Hispanics have significantly higher hepatic fat fractions (HFF) and slightly higher pancreatic fat fractions (not significant) than African Americans. However, the two groups have similar abdominal adipose tissue volumes. Due to their high HFFs, Hispanics are likely at a greater risk of obesity-related comorbidities.

At the University of Southern California, 3D IDEAL-MRI has been developed into a routine protocol and has been used by investigators to assess abdominal subcutaneous and visceral adipose tissue depot volumes and hepatic and pancreatic fat fraction in adolescents. The center has focused on comparing and contrasting these quantitative measures between genders and ethnicities. Figure 15 showcases results from a pilot study.

In summary, MR imaging and spectroscopy provide sensitive methods for detecting and quantifying adipose tissue volumes and ectopic fat fractions. Table 1 summarizes these methodologies and their principles. The quantitative fat endpoints achievable with each method are also listed. The reader is referred to three extensive review articles for additional details (Bley, 2010; Cassidy et al, 2009; Ma, 2008).

	Basis of Fat–Water Differentiation	Typical Dimensionality	Advantages	Disadvantages	Quantitative Endpoints
T_1-weighted MRI	T_1 relaxation	2D and 3D	strong fat-water tissue contrast, standard on all scanners, easy to implement, rapid scans	T_1 contrast varies with B_O field strength, requires protocol optimization	SAT and VAT volumes
Frequency-Selective MRI	chemical shift	2D and 3D	strong fat-water tissue contrast, option on most scanners, rapid scans	performance varies with B_O field strength and magnet inhomogeneity	SAT and VAT volumes
MR Spectroscopy (MRS)	chemical shift	single voxel	high spectral resolution of chemical profile, very accurate measure of fat to water fractions	limited coverage, requires expertise in protocol prescription, data collection and spectral analysis	ectopic fat fraction
Chemical Shift MRI	chemical shift	2D and 3D	complete fat-water tissue separation with accuracy comparable to MRS	not available on all scanners, requires special image reconstruction algorithms and protocol optimization for different B_O field strengths	SAT and VAT volumes, ectopic fat fraction

Table 1. Summary of MR imaging and spectroscopy methods for fat quantification.

4. Image analysis

In this section, procedures for extracting adipose tissue volumes and organ fat fractions from abdominal MRI data are discussed and illustrated using SliceOmatic software. The materials are presented in the context of abdominal imaging, but can be easily translated to other anatomies. The workflow for extracting fat measures from MRI data remains a daunting and costly task. It requires substantial data post-processing and analysis by an experienced operator. The steps involve the transfer of images to an offline workstation, followed by the use of dedicated software that typically require user involvement (Bonekamp et al., 2008). Free packages such as ImageJ, Osirix, and jMRUI (Naressi et al., 2001) and commercial programs such as SliceOmatic (Tomovision, Inc.), Analyze (AnalyzeDirect, Inc.) and Matlab (The Mathworks, Inc.) are commonly used for MRS analysis and image segmentation. Based on the author's experience, post-processing of a 3D abdominal MRI volume consisting of 60-80 slices can take approximately 45–60 minutes.

4.1 Subcutaneous and visceral adipose tissue

Since adipose tissue (SAT and VAT) is composed primarily of fat and its composition can be quite uniform, their identification and quantification in T_1-weighted, frequency-selective, and CSI data is straightforward. Single-voxel MRS can not be used since it does not provide anatomical data. For T_1 and frequency-selective approaches, a binary threshold is applied to the signal intensity of each voxel. Since fat is brighter, those voxels with intensities greater than the threshold are labeled as fat while those with lower intensities are excluded. Due to intensity variations that may arise across the image, the local threshold may need to be adjusted accordingly from region to region (Fig. 16). For CSI, the analysis can utilize the fat-only images and apply a similar threshold procedure. Alternatively, the analysis can exploit the fat fraction map where the signal intensity range is consistently fixed from 0–100%. Only voxels with fat fractions greater than a set value (e.g. 85%) are labeled as fat (Fig. 17).

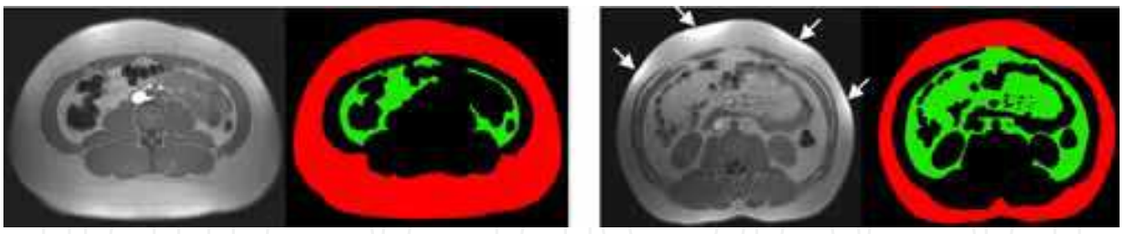

Fig. 16. Segmentation of SAT (red) and VAT (green) depots. Note the evident difference in VAT quantity between the two subjects. T_1-weighted images are shown. Arrows highlight artificial bright intensities caused by close proximity of the anatomy to receiver coils.

Regardless of the MRI technique, the operator usually needs to delineate the intra-abdominal boundary that separates SAT and VAT and the perimeter of the abdomen to exclude background air during segmentation. Additional exclusions of bowel contents, inter- and intra- muscular fat, spine and vertebrae, blood vessels, and other non-relevant structures are also required since some of these can have signal intensities that mimic fat. An area or volume measure is then computed for 2D multi-slice and contiguous 3D data based on the identified fat pixels/ voxels, respectively. With the exception of CSI fat fraction data that is always normalized between 0% and 100%, the operator must determine suitable thresholds on a subject-to-subject basis. This is necessary since signal intensities vary across

anatomy, subjects, examinations, and equipment and is usually not consistent. In SliceOmatic and Analyze, the operator has control over a sliding threshold and an interface that provides real time visual feedback on the performance of the chosen threshold.

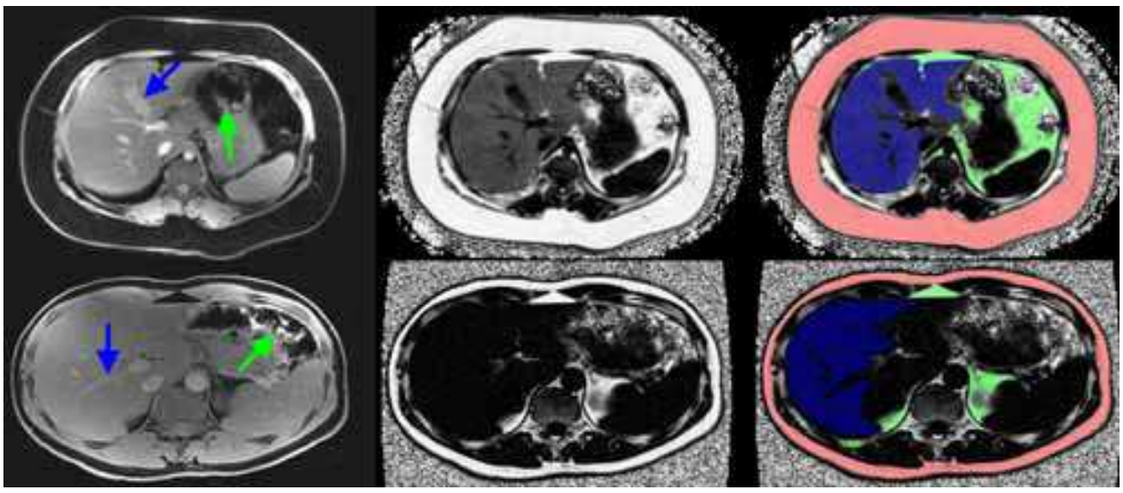

Fig. 17. IDEAL-based segmentation from two subjects, one with a fatty (top row) and one with a non-fatty (bottom row) liver. Water-only, fat fraction (0% black, 100% white) and overlay of segmentation (red: SAT, green: VAT, blue: liver) are shown in the left, middle, and right columns, respectively. The fuzzy noisy background in the fat fraction images has not been removed. In the fatty liver subject, note that hepatic vessels and the gall bladder (blue arrows) are well delineated in both water and fat fraction images, whereas in the non-fatty liver subject, such structures are only observable in the water image. Note that segmentation labels of the liver exclude these non-liver structures. VAT labels do not include erroneous signals from empty bowels (green arrows).

4.2 Ectopic fat

Ectopic fat quantification requires approaches that can separate water and fat signals within each voxel. Fat accumulation in organs and muscles can also be heterogenous. Therefore, the aforementioned binary threshold approach of "all fat" or "no fat" voxel classification is inadequate and only CSI methods are appropriate. Rather than measuring area or volume, a fraction of water and fat is computed. For MRS, the areas under the water and fat peaks can be calculated with software such as jMRUI. The MRS fat fraction is defined as the ratio of area under the fat peaks to the combined area of the water and fat peaks. CSI provides a fat fraction map across the imaging volume. The map is computed from the ratio of the reconstructed fat-only images to the sum of the water and fat images. To determine the fat fraction at a particular location, the operator simply draws a region-of-interest (ROI). The mean and standard deviation within the ROI is then computed. To quantify an organ, the operator must perform manual segmentation. Unlike single-voxel MRS, a volumetric fat fraction map affords immense flexibility. One can determine the average fat fraction across arbitrary ROI, including different lobes of the liver and the head and the tail of the pancreas. For accurate fat fractions, operator expertise is required for drawing ROIs and segmenting organs. In some cases, the fat fraction signal contrast surrounding abdominal organs may be poor, limiting an operator's ability to directly segment structures from the fat fraction maps

and visualize organ-muscle boundaries. This is particularly true for liver, pancreas, and kidneys with low fat content that appear visually similar to surrounding muscles. In these instances, the water-only, fat-only, in-phase, and out-of-phase data are used to provide anatomical landmarks and guide the segmentation. The operator can first segment from these images and transfer the ROIs to the corresponding fat fraction data (Fig. 18). The analysis of organ fat can account for more than 70% of post-processing time. The pancreas and the kidneys are also in close proximity to fat-rich VAT depots. An inaccurately drawn ROI meant to enclose only the organs may contain erroneous VAT voxels. In such cases, the high VAT fat fractions will significantly impact the apparent measured organ fat fraction.
In summary, post-processing by a trained operator is needed for computing quantitative fat endpoints. For SAT and VAT volumes, strong tissue contrast can facilitate intensity-based thresholding. The measurement of ectopic fat requires MRS and CSI. Manual segmentation demands familiarity with software and anatomy, as well as significant operator input.

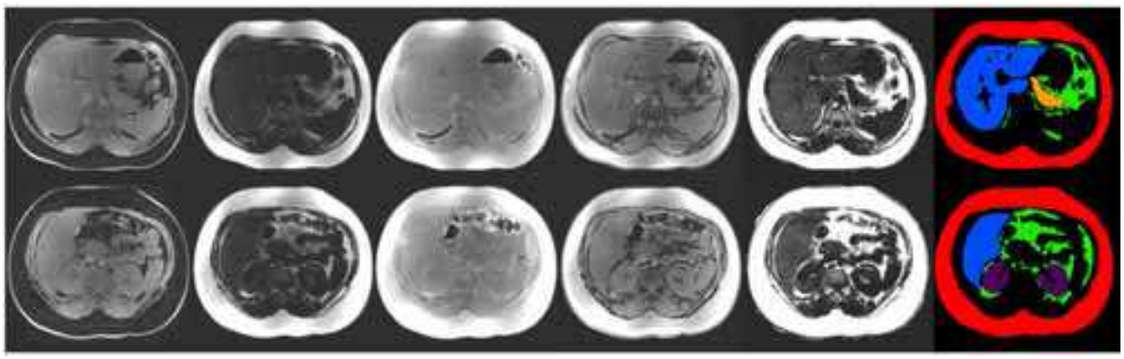

Fig. 18. Manual image segmentation from the full spectrum of IDEAL MRI data to delineate red: SAT, green: VAT, blue: liver, yellow: pancreas, purple: kidneys. Left to right: water-only, fat-only, in-phase, out-of-phase, fat fraction, and segmented labels from SliceOmatic.

5. Discussion

An investigator has several choices in MRI methods for body and organ fat assessment. In addition to selecting the appropriate technique, one must also consider tradeoffs between spatial resolution, scan time, and the need for breath-holds to minimize subject motion (Fig. 19). For MRS, 1–8 cm^3 voxels are commonly used. MRS requires a large voxel and several signal averages to yield a clean spectrum. Prescription of MRS voxels during an examination requires operator expertise such that placement of the voxel does not contain any undesired tissues. Motion from the subject or shifting of organs due to respiration or peristalsis after voxel placement can lead to spatial misalignments and unrealistic measurements (Hu et al., 2010). Respiration should be monitored with a bellows transducer for data synchronization. Alternatively, multiple and consistent breath-holds can be used with clear instructions given to the patient. In practice, these MRS approaches may not be possible in subjects with a large abdominal circumference or who have difficulties with breath-holds.
Resolutions for imaging approaches are on the order of millimeters. While small voxels are desirable for visualizing anatomical detail, it leads to increased scan times and lowers image signal-to-noise ratio. Long scan times also increase the risk of motion and blurring artifacts. In CSI, blurring artifacts from respiration can further cause unrealistic fat

fraction distributions within organs and at organ-fat interfaces. High spatial resolution scans also necessitate breath-holding, which may not be well-tolerated by children, uncooperative or obese subjects. Spatial resolution is determined by the FOV and the acquisition matrix, the number of slices, the slice thickness, and the inter-slice gap, if any. These parameters are freely chosen by the operator, can impact scan time, and are dependent on body habitus.

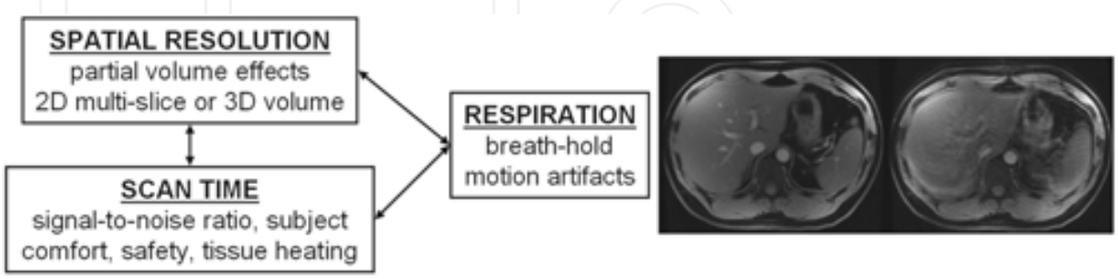

Fig. 19. Practical imaging parameters and considerations in MRI. In designing an appropriate protocol, one must consider the desired quantitative endpoints and leverage spatial resolution, scan time, patient safety, and the need for breath-holding. Image pair shows a slice of the liver in the same subject with (left) and without breath-holding (right).

The investigator and operator must also choose between 2D multi-slice or 3D volumetric pulse sequences. With 2D techniques, data are acquired on a slice-by-slice format such that data obtained for one slice is independent of any other slice. Subject motion and artifacts are generally not an issue in 2D methods. The time needed to acquire each slice is very short, requiring sub-seconds to a few seconds. The technique also allows the operator to specify a gap between non-contiguous adjacent slices. While this appears attractive in terms of scan efficiency, large inter-slice gaps and thick (~10 mm) slices can lead to partial volume errors and impact quantitative accuracy, especially in SAT and VAT depots. They are also difficult to generate subsequent 3D rendered visualizations (Fig. 20).

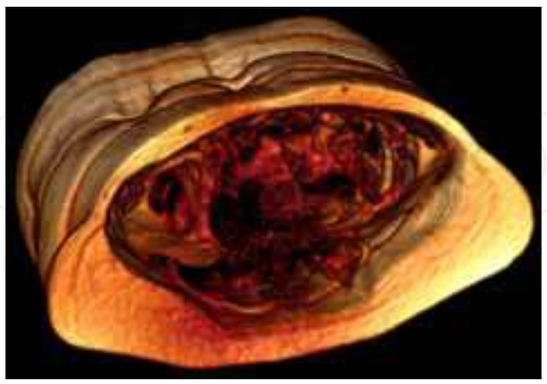

Fig. 20. Volume-rendered IDEAL MRI fat series, illustrating the contiguous 3D data set. The volume consists of 36 native 5-mm axial slices, obtained with three 15-sec breath-holds.

In contrast, 3D approaches acquire data that represent the entire volume. Volumetric imaging implies contiguous coverage and no inter-slice gaps. Given similar imaging parameters and coverage, 3D protocols often contain more slices, have longer scan times,

and are more susceptible to motion than 2D approaches. However, since signals arise from a larger volume rather than a smaller slice, 3D methods exhibit greater signal-to-noise ratios. Breath-holding or respiratory gating is often required for abdominal 3D sequences. Three-dimensional approaches also offer intrinsic advantages over 2D methods, such as greater parallel imaging acceleration rates and more robust parallel imaging performance to reduce scan time. Parallel imaging is a topic beyond the scope of this chapter, and the reader is referred to the literature for details (Margolis et al., 2004). Other 3D benefits include thinner slices (sub-millimeter) and the ability to accommodating preparatory RF pulses that further enhance T_1 and fat to lean tissue contrast.

Lastly, for a given set of spatial resolutions and imaging parameters used in abdominal imaging, scan times in T_1-weighted, frequency-selective, MRS, and CSI approaches should be comparable between 1.5 and 3 Tesla protocols. In some instances, safety and RF tissue heating limits may lengthen 3 Tesla protocol durations over their 1.5 Tesla counterparts. At higher B_0 field strengths, greater chemical shift differences can also cause CSI sequences to increase in scan time due to shorter in-phase and out-of-phase echo periodicities.

In the literature, 2–4 mm in-plane resolution and a slice thickness between 5–10 mm have been reported for SAT and VAT quantification. For 2D multi-slice approaches inter-slice gaps as wide as 10 mm have been reported. Since the determination of volumes rely on thresholding and an "all fat" or "no fat" labeling each voxel, any incorrect labeling can lead to substantial quantification errors when using large voxels. Large voxels also generate partial volume effects where many can encompass both fat and lean tissues. These voxels exhibit ambiguous signal intensities that can cause threshold errors. Similarly, low spatial resolution and thick slices containing both organ and adjacent fat can exhibit unrealistic CSI fat fractions. There has been a transition in recent studies to adopt contiguous 2D multi-slice approaches with thin slices (Siegel et al., 2007) and 3D protocols (Berglund et al., 2010; Bornert et al., 2007; Kullberg et al., 2009).

For final consideration, modern MRI platforms are equipped with receiver arrays designed specifically for abdominal imaging. The array is strapped to the subject to provide high signal-to-noise ratios. However, they also create signal intensity variations across the imaging volume. If possible, these variations should be corrected with software from MRI vendors prior to image analysis. One attractive feature of CSI fat fraction maps is that they are generated as a ratio of water and fat images. While the individual source images may exhibit signal variations, their ratio removes the bias. The use of arrays may be limited in obese subjects as they are unable to fit within the magnet bore with the receivers strapped.

6. Future directions and conclusion

The design of appropriate MRI protocols for fat assessment requires considerations of the desired quantitative endpoints and tradeoffs in the imaging parameters. Other practical issues include body sizes of the cohort and the cost and throughput efficiency of the study. The usage cost associated with MRI can range from $300 to $600 per hour in a typical clinical radiology department. Regardless of the study, overhead time is always required for setup and for giving instructions to the subject. T_1-weighted and frequency-selective approaches are very fast and typically require only a few seconds per slice for data acquisition. Whole-abdomen coverage with these sequences takes only a few minutes of actual scan time and is generally considered as a first option for SAT and VAT quantification. In our experience,

utilizing only these sequences, an exam can be comfortably completed in 10 minutes. If ectopic fat fractions are needed, either a MRS or CSI protocol is then added. The MRS sequence necessitates significant user interaction, preparation work, and operator time. In our experience, MRS per single voxel takes approximately 5 minutes. The further addition of a 3D whole-abdomen CSI protocol such as IDEAL will require 5–7 more breath-holds, bringing the total examination time from setup to patient removal to 30–45 minutes.

% difference in volume	SAT	VAT	Liver	Pancreas
Intra-Rater Comparison (11 subjects, 4 segmentations)				
Mean	-0.86	1.41	-0.13	-0.40
Range	-4.97 to 1.53	-8.34 to 4.47	-5.48 to 6.18	-6.66 to 5.00
Inter-Rater Comparison (7 subjects, 2 segmentations)				
Mean	1.32	1.20	-0.84	1.23
Range	-1.30 to 5.48	-6.05 to 5.64	-6.07 to 5.69	-5.21 to 9.95

Table 2. Percent difference in segmented volumes of fat depots and organs in two scenarios, as part of routine quality control performed at our institution. In the first, a single operator segmented 11 data sets, each 4 times, in random order. In the second, two independent operators, in a blinded format, segmented 7 data sets in random order. Note that the mean differences are all less than 2%, signifying excellent segmentation consistency.

Despite its rapid growth, MRI remains an untapped resource in obesity research and has not yet reached its full potential. Many opportunities remain for future investigation. Several groups have recognized the time-consuming and labor-intensive work involved with manual image segmentation. This can be daunting in longitudinal studies, as the process must be performed for every scan at multiple time points across the same subject. Efficient semi-automated and automated algorithms have been proposed, but are usually limited to in-house usage (Armao et al., 2006; Demerath et al., 2007; Kullberg et al., 2010; Peng et al., 2007; Positano et al., 2004; Wilhelm Poll et al., 2003). Techniques that can automatically segment adipose tissue and organs from a subject's MRI data at subsequent time points while utilizing *a priori* information from the same subject's baseline segmentations are being explored. The capability of achieving rapid intra-subject 3D registration, segmentation, and quantification will provide investigators with detailed person-specific information reflecting the temporal change in fat distribution and volumes in response to intervention. Such capability will also exploit the richness of 3D MRI that is unavailable in gapped 2D multi-slice data. Quality control will be essential in assuring consistency and accuracy. Fat measurements should be routinely validated against phantoms, between multiple blinded observers, and between manual and automated segmentations (Table 2). There are only a few literature reports describing the accuracy and repeatability of quantitative fat MRI.

In conclusion, MRI is the most powerful and comprehensive imaging tool for fat quantification. With CSI methods, recent studies are beginning to demonstrate their usefulness and investigators are exploring new fat biomarkers and associations in obesity

with MRI that were previously untapped. This chapter has provided introductory materials for investigators to survey, understand, and integrate MRI into their studies.

7. Acknowledgment

The authors are grateful to the faculty and staff of the Childhood Obesity Research Center at the University of Southern California for research assistance, particularly Sherryl Esplana Rosa Rangel, Christina Ayala, and Kami McClure. The authors acknowledge Huanzhou Yu, Ph.D., Ann Shimakawa, M.S., and Jean Brittain, Ph.D., from GE Healthcare for technical and research support. The authors thank Gavin Hamilton, Ph.D., from the University of California San Diego for assistance with MRS, and Mark Punyanitya and Wei Shen, M.D., from Columbia University, for assistance with SliceOmatic. Finally, the authors acknowledge Daniel L. Smith, Jr., Ph.D, and Timothy R. Nagy, Ph.D., from the University of Alabama at Birmingham for recognizing the potential of IDEAL with brown adipose tissue.

8. References

Abate N, Garg A, Coleman R, Grundy SM, & Peshock RM. (1997). Prediction of total subcutaneous abdominal, intraperitoneal, and retroperitoneal adipose tissue masses in men by single axial magnetic resonance imaging slice. *American Journal of Clinical Nutrition*, Vol. 65, No. 2, February 1997, pp. 403-408.

Armao D, Guyon JP, Firat Z, Brown MA, & Semelka RC. (2006). Accurate quantification of visceral adipose tissue (VAT) using water-saturation MRI and computer segmentation: preliminary results. *Journal of Magnetic Resonance Imaging*, Vol. 23, No. 5, May 2006, pp. 736-741.

Berglund J, Johansson L, Ahlstrom H, & Kullberg J. (2010). Three-point Dixon method enables whole-body water and fat imaging of obese subjects. *Magnetic Resonance in Medicine*, Vol. 63, No. 6, June 2010, pp. 1659-1668.

Berglund J, Ahlstrom H, Johansson L, & Kullberg J. (2011). Two-point Dixon method with flexible echo times. *Magnetic Resonance in Medicine*, Vol. 65, No. 4, April 2011, pp. 994-1004.

Bernard CP, Liney GP, Manton DJ, Turnbull LW, & Langton, CM. (2008). Comparison of fat quantification methods: a phantom study at 3.0T. *Journal of Magnetic Resonance Imaging*, Vol. 27, No. 1, January, pp. 192-197.

Bernstein MA, King K, & Zhou X. (2004). *Handbook of MRI pulse sequences* (1st edition), Elsevier Academic Press, ISBN 0-12-092861-2, Amsterdam.

Bley TA, Wieben O, Francois CJ, Brittain JH, & Reeder SB. (2010). Fat and water magnetic resonance imaging. *Journal of Magnetic Resonance Imaging*, Vol. 31, No. 1, January 2010, pp. 4-18.

Bonekamp S, Ghosh P, Crawford S, Solga SF, Horska A, Brancati FL, Diehl AM, Smith S, & Clark JM. (2008). Quantitative comparison and evaluation of software packages for assessment of abdominal adipose tissue distribution by magnetic resonance imaging. *International Journal of Obesity*, Vol. 32, No. 1, January 2008, pp. 100-111.

Bornert P, Keupp J, Eggers H, & Aldefeld B. (2007). Whole-body 3D water/ fat resolved continuously moving table imaging. *Journal of Magnetic Resonance Imaging*, Vol. 25, No. 3, March 2007, pp. 660-665.

Brix G, Heiland S, Bellemann ME, Koch T, & Lorenz WJ. (1993). MR imaging of fat-containing tissue : valuation of two quantitative imaging techniques in comparison to localized proton spectroscopy. *Magnetic Resonance Imaging*, Vol. 11, No. 7, pp. 977-991.

Bydder M, Yokoo T, Hamilton G, Middleton MS, Chavez AD, Schwimmer JB, Lavine JE, & Sirlin CB. (2008). Relaxation effects in the quantification of fat using gradient echo imaging. *Magnetic Resonance in Medicine*, Vol. 26, No. 3, January 2008, pp. 347-359.

Bydder M, Yokoo T, Yu H, Carl M, Reeder SB, & Sirlin CB. (2011). Constraining the initial phase in water-fat separation. *Magnetic Resonance Imaging*, Vol. 29, No. 2, February 2011, pp. 216-221.

Cassidy FH, Yokoo T, Aganovic L, Hanna RF, Bydder M, Middleton MS, Hamilton G, Chavez AD, Schwimmer JB, & Sirlin CB. (2009). Fatty liver disease: MR imaging techniques for the detection and quantification of liver steatosis. *Radiographics*, Vol. 29, No. 1, January-February 2009, pp. 231-260.

Chebrolu VV, Hines CDG, Yu H, Pineda AR, Shimakawa A, McKenzie CA, Samsonov A, Brittain JH, & Reeder SB. (2010). Independent estimation of T2* for water and fat for improved accuracy of fat quantification. Vol. 63, No. 4, April 2010, pp. 849-857.

Choudhary AK, Donnelly LF, Racadio JM, & Strife JL. (2007). Diseases associated with childhood obesity. *Americain Journal of Roentgenology*, Vol. 188, No. 4, April 2007, pp. 1118-1130.

De Bazelaire CM, Duhamel GD, Rofsky NM, & Alsop DC. (2004). MR imaging relaxation times of abdominal and pelvic tissues measured in vivo at 3.0T : preliminary results. *Radiology*, Vol. 230, No. 3, March 2004, pp. 652-659.

Demerath EW, Ritter KJ, Couch WA, Rogers NL, Moreno GM, Choh A, Lee M, Remsberg K, Czerwinski SA, Chumlea WC, Siervogel RM, & Towne B. (2007). Validity of a new automated software program for visceral adipose tissue estimation. *International Journal of Obesity*, Vol. 31, No. 2, February 2007, pp. 285-291.

Despres JP, Lemieux I, Bergeron J, Pibarot P, Mathieu P, Larose E, Rodes-Cabau J, Bertrand OF, & Poirier P. (2008). Abdominal obesity and the metabolic syndrome : contribution to global cardiometabolic risk. *Arteriosclerosis, Thrombosis, and Vascular Biology*, Vol. 28, No. 6, June 2008, pp. 1039-1049.

Eggers H, Brendel B, Duijndam A, & Herigault G. (2011). Dual-echo Dixon imaging with flexible choice of echo times. *Magnetic Resonance in Medicine*, Vol. 65, No. 1, January 2011, pp. 96-107.

Ellis KJ. Human body composition, in vivo methods. (2000). *Physiological Review*, Vol. 80, No. 2, April 2000, pp. 649-680.

Flegal KM, Caroll MD, Odgen CL, & Curtin LR. Prevalence and trends in obesity among US adults, 1999-2008. (2010). *Journal of the American Medical Association*, Vol. 303, No. 3, January 2010, pp. 235-241.

Goodpaster BH, Thaete FL, & Kelley DE. Composition of skeletal muscle evaluated with computed tomography. (2000). *Annals of New York Academy of Sciences*, Vol. 904, May 2000, pp. 18-24.

Guiu B, Petit JM, Loffroy R, Ben Salem D, Aho S, Masson D, Hillon P, Krause D, & Cercueil JP. (2009). Quantification of liver fat content: comparison of triple-echo chemical shift gradient-echo imaging and in vivo proton MR spectroscopy. *Radiology*, Vol. 250, No. 1, January 2009, pp. 95-102.

Haacke EM, Brown RW, Thompson MR, & Venkatesan R. (1999). *Magnetic resonance imaging, physical principles and sequence design* (1st edition), John Wiley and Sons, Inc., ISBN 0-471-35128-8, New York.

Hamilton G, Middleton MS, Bydder M, Yokoo T, Schwimmer JB, Kono Y, Patton HM, Lavine JE, & Sirlin CB. (2009). Effect of PRESS and STEAM sequences on magnetic resonance spectroscopic liver fat quantification. *Journal of Magnetic Resonance Imaging*, Vol. 30, No. 1, July 2009, pp. 145-152.

Hashemi RH, & Bradley, Jr. WG. (1997). *MRI the basics* (1st edition), Lippincott Williams and Wilkins, ISBN 0-683-18240-4, Philadelphia.

Hernando D, Liang ZP, Kellman P. (2010). Chemical shift-based water/ fat separation : a comparison of signal models. *Magnetic Resonance in Medicine*, Vol. 64, No. 3, September 2010, pp. 811-822.

Hines CDG, Yu H, Shimakawa A, McKenzie CA, Brittain JH, & Reeder SB. (2009). T1 independent, T2* corrected MRI with accurate spectral modeling for quantification of fat: validation in a fat-water-SPIO phantom. *Journal of Magnetic Resonance Imaging*, Vol. 30, No. 5, November 2009, pp. 1215-1222.

Hood MN, & Ho VB. (1999). Chemical shift : the artifact and clinical tool revisited. *Radiographics*, Vol. 19, No. 2, March-April 1999, pp. 357-371.

Hu HH, Kim HW, Nayak KS, & Goran MI. (2010). Comparison of fat-water MRI and single-voxel MRS in the assessment of hepatic and pancreatic fat fractions in humans. *Obesity*, Vol. 18, No. 4, April 2010, pp. 841-847.

Hu HH, Smith DL, Jr., Nayak KS, Goran MI, & Nagy TR. (2010). Identification of brown adipose tissue in mice with fat-water IDEAL-MRI. *Journal of Magnetic Resonance Imaging*, Vol. 31, No. 5, May 2010, pp. 1195-1202.

Jackson AS, & Pollock ML. (1982). Steps toward the development of generalized equations for predicting body composition of adults. *Canadian Journal of Applied Sport Science*, Vol. 7, No. 3, September 1982, pp. 189-196.

Kaldoudi E, Williams SC, Barker GJ, & Tofts PS. (1993). A chemical shift selective inversion recovery sequence for fat-suppressed MRI: theory and experimental validation. *Magnetic Resonance Imaging*, Vol. 11, No. 3, March 1993, pp. 341-355.

Kellman P, Hernando D, & Arai AE. (2010). Myocardial fat imaging. *Current Cardiovascular Imaging Reports*, Vol. 3, No. 2, April 2010, pp. 83-91.

Kim H, Taksali SE, Dufour S, Befroy D, Goodman TR, Petersen KF, Shulman GI, Caprio S, & Constable RT. (2008). Comparative MR study of hepatic fat quantification using single-voxel proton spectroscopy, two-point Dixon and three-point IDEAL. *Magnetic Resonance in Medicine*, Vol. 59, No. 3, March 2008, pp. 521-527.

Kullberg J, Johansson L, Ahlstrom H, Courivaud F, Koken P, Eggers H, & Bornert P. (2009). Automated assessment of whole-body adipose tissue depots from continuously moving bed MRI: a feasibility study. *Journal of Magnetic Resonance Imaging*, Vol. 31, No. 1, July 2009, pp. 185-193.

Kullberg J, Brandberg J, Angelhed JE, Frimmel H, Bergelin E, Strid L, Ahlstrom H, Johansson L, & Lonn L. (2009). Whole-body adipose tissue analysis: comparison of MRI, CT and dual energy X-ray absorptiometry. *British Journal of Radiology*, Vol. 82, No. 974, February 2009, pp. 123-130.

Kullberg J, Karlsson AK, Stokland E, Svensson PA, & Dahlgren J. (2010). Adipose tissue distribution in children: automated quantification using water and fat MRI. *Journal of Magnetic Resonance Imaging,* Vol. 32, No. 1, July 2010, pp. 204-210.

Kvist H, Chowdhury B, Grangard U, Tylen U, & Sjostrom L. (1988). Total and visceral adipose-tissue volumes derived from measurements with computed tomography in adult men and women : predictive equations. *American Journal of Clinical Nutrition*, Vol. 48, No. 6, December 1988, pp. 1351-1361.

Lancaster JL, Ghiatas AA, Alyassin A, Kilcoyne RF, Bonora E, & DeForonzo RA. (1991). Measurement of abdominal fat with T_1-weighted MR images. *Journal of Magnetic Resonance Imaging*, Vol. 1, No. 3, May-June, pp. 363-369.

Lingvay I, Esser V, Legendre JL, Price AL, Wertz KM, Adams-Huet B, Zhang S, Unger RH, & Szczepaniak LS. (2009). Noninvasive quantification of pancreatic fat in humans. *Journal of Clinical Endocrinology and Metabolism*, Vol. 94, No. 10, October 2009, pp. 4070-4076.

Liu CY, McKenzie CA, Yu H, Brittain JH, & Reeder SB. (2007). Fat quantification with IDEAL gradient echo imaging: correction of bias from T1 and noise. *Magnetic Resonance in Medicine*, Vol. 58, No. 2, August, pp. 354-364.

Ma J, Slavens Z, Sun W, Bayram E, Estowski L, Hwang KP, Akao J, & Vu AT. (2008). Linear phase-error correction for improved water and fat separation in dual-echo Dixon techniques. *Magnetic Resonance in Medicine*, Vol. 60, No. 5, November 2008, pp. 1250-1255.

Ma J. (2008). Dixon techniques for water and fat imaging. *Journal of Magnetic Resonance Imaging*, Vol. 28, No. 3, September 2008, pp. 543-558.

Machann J, Bachmann OP, Brechtel K, Dahl DB, Wietek B, Klumpp B, Haring HU, Claussen CD, Jacob S, & Schick F. (2003). Lipid content in the musculature of the lower leg assessed by fat selective MRI: intra- and interindividual differences and correlation with anthropometric and metabolic data. *Journal of Magnetic Resonance Imaging*, Vol. 17, No. 3, March 2003, pp. 350-357.

Machann J, Thamer C, Schnoedt B, Haap M, Haring HU, Claussen CD, Stumvoll M, Fritsche A, & Schick F. (2005). Standardized assessment of whole body adipose tissue topography by MRI. *Journal of Magnetic Resonance Imaging*, Vol. 21, No. 4, April 2005, pp. 455-462.

Margolis DJ, Bammer R, & Chow LC. (2004). Parallel imaging of the abdomen. *Topics in Magnetic Resonance Imaging*, June 2004, Vol. 15, No. 3, pp. 197-206.

Mattsson S, & Thomas BJ. Development of methods for body composition studies. (2006). *Physics in Medicine and Biology*, Vol. 51, No. 13, July 2006, pp. R203-R228.

Meisamy S, Hines CD, Hamilton G, Sirlin CB, McKenzie CA, Yu H, Brittain JH, & Reeder SB. (2011). Quantification of hepatic steatosis with T1-independent, T2* corrected MR imaging with spectral modeling of fat : blinded comparison with MR spectroscopy. *Radiology*, Vol. 258, No. 3, March 2011, pp. 767-775.

Napolitano A, Miller SR, Murgatroyd PR, Coward WA, Wright A, Finer N, De Bruin TW, Bullmore ET, & Nunez DJ. Validation of a quantitative magnetic resonance method. (2008). *Obesity*, Vol. 16, No. 1, January 2008, pp. 191-198.

Naressi A, Couturier C, Castang I, de Beer R, & Graveron-Demilly D. (2001). Java-based graphical user interface for MRUI, a software package for quantitation of in

vivo/ medical magnetic resonance spectroscopy signals. *Computers in Biology and Medcine*, Vol. 31, No. 4, July 2001, pp. 269-286.

O'Regan DP, Callaghan MF, Wylezinska-Arridge M, Fitzpatrick J, Naoumova RP, Hajnal JV, & Schmitz SA. (2008). Liver fat content and T2*: simultaneous measurement by using breath-hold multiecho MR imaging at 3.0 T--feasibility. *Radiology*, Vol. 247, No. 2, May 2008, pp. 550-557.

Peng Q, McColl RW, Ding Y, Wang J, Chia JM, & Weatherall PT (2007). Automated method for accurate abdominal fat quantification on water-saturated magnetic resonance images. *Journal of Magnetic Resonance Imaging*, Vol. 26, No. 3, September 2007, pp. 738-746.

Positano V, Gastaldelli A, Sironi AM, Santarelli MF, Lombardi M, & Landini L. (2004). An accurate and robust method for unsupervised assessment of abdominal fat by MRI. *Journal of Magnetic Resonance Imaging*, Vol. 20, No. 4, October 2004, pp. 684-689.

Ren J, Dimitrov I, Sherry AD, & Malloy CR. (2008). Composition of adipose tissue and marrow fat in humans by 1H NMR at 7 Tesla. *Journal of Lipid Research*, Vol. 49, No. 9, September 2008, pp. 2055-2062.

Reeder SB, McKenzie CA, Pineda AR, Yu H, Shimakawa A, Brau AC, Hargreaves BA, Gold GE, & Brittain JH. (2007). Water-fat separation with IDEAL gradient-echo imaging. *Journal of Magnetic Resonance Imaging*, Vol. 25, No. 3, March 2007, pp. 644-652.

Reeder SB, Robson PM, Yu H, Shimakawa A, Hines CD, McKenzie CA, & Brittain JH. (2009). Quantification of hepatic steatosis with MRI: the effects of accurate fat spectral modeling. *Journal of Magnetic Resonance Imaging*, Vol. 29, No. 6, May 2009, pp. 1332-1339.

Reeder SB, & Sirlin CB. (2010). Quantification of liver fat with magnetic resonance imaging. *Magnetic Resonance Imaging Clinics of North America*, Vol. 18, No. 3, August 2010, pp. 337-357.

Ross R, Goodpaster B, Kelley D, & Boada F. (2000). Magnetic resonance imaging in human body composition research: from quantitative to qualitative tissue measurement. *Annals of New York Academy of Sciences*, Vol. 904, May 2000, pp. 12-17.

Seidell JC, Bakker CJ, & van der Kooy K. Imaging techniques for measuring adipose-tissue distribution—a comparison between computed tomography and 1.5T magnetic resonance. (1990). *American Journal of Clinical Nutrition*, Vol. 51, No. 6, June 1990, pp. 953-957.

Schick F, Machann J, Brechtel K, Strempfer A, Klumpp B, Stein DT, & Jacob S. (2002). MRI of muscular fat. *Magnetic Resonance in Medicine*, Vol. 47, No. 4, April 2002, pp. 720-727.

Siegel MJ, Hildebolt CF, Bae KT, Hong C, & White NH. (2007). Total and intraabdominal fat distribution in preadolescents and adolescents: measurement with MR imaging. *Radiology*, Vol. 242, No. 3, March 2007, pp. 846-856.

Stanisz GJ, Odrobina EE, Pun J, Escaravage M, Graham SJ, Bronskill MJ, & Henkelman RM. (2005). T1, T2 relaxation and magnetization transfer in tissue at 3T. *Magnetic Resonance in Medicine*, Vol. 54, No. 3, September 2005, pp. 507-512.

Thomas EL, Hamilton G, Patel N, O'Dwyer R, Dore CJ, Goldin RD, Bell JD, & Taylor-Robinson, SD. (2005). Hepatic triglyceride content and its relation to body adiposity: a magnetic resonance imaging and proton magnetic resonance spectroscopy study. *Gut*, Vol.54, No. 1, January 2005, pp. 122-127.

van Werven JR, Hoogduin JM, Nederveen AJ, van Vliet AA, Wajs E, Vandenberk P, Stroes ES, & Stoker J. (2009). Reproducibility of 3.0 Tesla magnetic resonance spectroscopy for measuring hepatic fat content. *Journal of Magnetic Resonance Imaging*, Vol. 30, No. 2, August 2009, pp. 444-448.

Vlaardingerbroek MT, & den Boer JA. (1999). *Magnetic resonance imaging* (2nd edition), Springer, ISBN 3-540-64877-1, Berlin.

Weis J, Johansson L, Ortiz-Nieto F, & Ahlstrom H. (2008). Assessment of lipids in skeletal muscle by high-resolution spectroscopic imaging using fat as the internal standard: Comparison with water referenced spectroscopy. *Magnetic Resonance in Medicine*, Vol. 59, No. 6, June 2008, pp. 1259-1265.

Wilhelm Poll L, Wittsack HJ, Koch JA, Willers R, Cohnen M, Kapitza C, Heinemann L, & Modder U. (2003). A rapid and reliable semi automated method for measurement of total abdominal fat volumes using magnetic resonance imaging. *Magnetic Resonance Imaging*, Vol. 21, No. 6, July 2003, pp. 631-636.

Xiang, QS. (2006). Two-point water-fat imaging with partially-opposed-phase (POP) acquisition: an asymmetric Dixon method. *Magnetic Resonance in Medicine*, Vol. 56, No. 3, September 2006, pp. 572-584.

Yokoo T, Bydder M, Hamilton G, Middleton MS, Gamst AC, Wolfson T, Hassanein T, Patton HM, Lavine JE, Schwimmer JB, & Sirlin CB. (2009). Nonalcoholic fatty liver disease: diagnostic and fat-grading accuracy of low-flip-angle multiecho gradient-recalled-echo MR imaging at 1.5 T. *Radiology*, Vol. 251, No. 1, April 2009, pp. 67-76.

Yu H, Shimakawa A, McKenzie CA, Brodsky E, Brittain JH, & Reeder SB. (2008). Multiecho water-fat separation and simultaneous R2* estimation with multifrequency fat spectrum modeling. *Magnetic Resonance in Medicine*, Vol. 60, No. 5, November 2008, pp. 1122-1134.

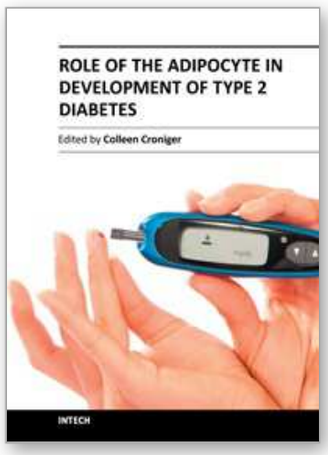

Role of the Adipocyte in Development of Type 2 Diabetes

Edited by Dr. Colleen Croniger

ISBN 978-953-307-598-3
Hard cover, 372 pages
Publisher InTech
Published online 22, September, 2011
Published in print edition September, 2011

Adipocytes are important in the body for maintaining proper energy balance by storing excess energy as triglycerides. However, efforts of the last decade have identified several molecules that are secreted from adipocytes, such as leptin, which are involved in signaling between tissues and organs. These adipokines are important in overall regulation of energy metabolism and can regulate body composition as well as glucose homeostasis. Excess lipid storage in tissues other than adipose can result in development of diabetes and nonalcoholic fatty liver disease (NAFLD). In this book we review the role of adipocytes in development of insulin resistance, type 2 diabetes and NAFLD. Because type 2 diabetes has been suggested to be a disease of inflammation we included several chapters on the mechanism of inflammation modulating organ injury. Finally, we conclude with a review on exercise and nutrient regulation for the treatment of type 2 diabetes and its co-morbidities.

InTech Europe
University Campus STeP Ri
Slavka Krautzeka 83/A
51000 Rijeka, Croatia
Phone: +385 (51) 770 447
Fax: +385 (51) 686 166
www.intechopen.com

InTech China
Unit 405, Office Block, Hotel Equatorial Shanghai
No.65, Yan An Road (West), Shanghai, 200040, China
中国上海市延安西路65号上海国际贵都大饭店办公楼405单元
Phone: +86-21-62489820
Fax: +86-21-62489821

IntechOpen